

**Transition model for ricin-aptamer interactions with multiple pathways and energy barriers**

Bin Wang and Bingqian Xu\*

*Single Molecule Study Laboratory, College of Engineering and Nanoscale Science and Engineering Center, University of Georgia, Athens, Georgia 30602, USA*

(Received 18 December 2012; revised manuscript received 7 November 2013; published 24 February 2014)

We develop a transition model to interpret single-molecule ricin-aptamer interactions with multiple unbinding pathways and energy barriers measured by atomic force microscopy dynamic force spectroscopy. Molecular simulations establish the relationship between binding conformations and the corresponding unbinding pathways. Each unbinding pathway follows a Bell-Evans multiple-barrier model. Markov-type transition matrices are developed to analyze the redistribution of unbinding events among the pathways under different loading rates. Our study provides detailed information about complex behaviors in ricin-aptamer unbinding events.

DOI: [10.1103/PhysRevE.89.022720](https://doi.org/10.1103/PhysRevE.89.022720)

PACS number(s): 87.14.gk, 82.20.Db, 82.37.Np, 87.64.Dz

**I. INTRODUCTION**

Interactions between proteins and nucleic acids are critical to many biophysical processes in living cells such as gene expression, DNA repair, and cell replication [1,2]. For most of these interactions the nucleic acids show complex behaviors such as flexible folding structures, multiple energy barriers, and multiple reaction pathways for the same ligand-receptor system. Single-molecule measurements provide structural and functional information of biomolecules participating in these reactions [3–5]. Biophysical theories developed by Bell, Evans, and Jarzynski have been used to estimate the binding free energy at the equilibrium state from nonequilibrium measurements [6–8]. However, while dealing with complex systems, including the unbinding processes of protein and nucleic acids, issues related to multiple energy barriers and reaction pathways have to be considered. Recently, the biophysical research community has given increasing attention to multiple-bond folding (unfolding) and binding (unbinding) reactions [9–15]. Nonetheless, detailed binding-unbinding mechanisms for such complex systems require further investigation [4,16]. To quantitatively study the specific behaviors of reaction networks, practical biophysical models revealing the relationship between the molecular structures and their behaviors are crucial.

Here we develop a practical transition model for the reaction network of ricin-aptamer interactions. This model combined the Bell-Evans model and Markov-type transition matrices to explain complex relationships among the molecular structures, unbinding forces, and activation energies, using data obtained by atomic force microscopy-dynamic force spectroscopy (AFM-DFS) [Fig. 1(a)]. DNA or RNA aptamers are short sequences of single-strand DNA or RNA having interactions specific to their target species. These targets include certain proteins or biomolecules involved in essential processes of living cells or some cytotoxic species that can cause diseases or cell death [16]. One of these cytotoxic species is ricin, which interacts with adenine in ribosomes and inhibits protein synthesis in living cells [17]. We have previously reported the AFM and DFS measurements of ricin conformations and its interactions with another aptamer of simpler folding structure [18].

In this study, multiple unbinding forces have been observed under a similar extension distance in force-distance  $f$ - $d$  curves [Fig. 1(b) inset]. This phenomenon indicated that more than one unbinding pathway might exist for the aptamer-ricin interactions [Fig. 1(b)]. Shifting of force distributions in the histograms under different loading rates suggested that these multiple unbinding pathways follow the Bell-Evans model (Fig. 2). An appropriate quantitative model to explain these observed experimental results is the Markov chain, which relates the peak areas to the likelihoods of unbinding reactions. Therefore, the changes of peak areas in the force histograms under different loading rates reflect the redistributions of individually measured unbinding forces, which connect to each reaction pathway. The Markov-type transition matrix is a unique tool to connect multiple unbinding pathways in an overall mathematical expression. A specialized transition matrix can be built according to the reaction network formed by the multiple pathways. Then this Markov-type model can be used to quantitatively investigate the force redistribution processes (i.e., the force transitions) happening under different loading rates.

The aptamer we use is a sequence of DNA predicted to have two major hairpin-loop structures: loops I and III [16]. We find that ricin-aptamer interactions happen in three different binding sites. The aptamer loop I or III can bind to its own binding site on the ricin surface. Loops I and III can also simultaneously bind to ricin on a different binding site [Figs. 1(c)–1(e)] [19,20]. In our DFS experiments, the aptamer is attached to a long polyethylene glycol (PEG) linker, while the ricin molecules are in a very low surface concentration. Therefore, the aptamer can easily reach the individual ricin molecules with all of their binding sites and loops. This experimental design increases the probability of multiple-bond binding and unbinding. The force values of this third peak varies from 69.6 to 101.2 pN while the loading rate changed from 0.24 to 51.64 nN s<sup>-1</sup>. These loading rates and forces values are in the same ranges people used in other DFS studies of multiple-bond reactions [9,21–23]. These three different binding complexes correspond to three different unbinding pathways and show specific distributions in the histograms of unbinding forces [Figs. 2(a)–2(j)]. These three unbinding pathways each have individual energy profiles and one unbinding reaction (one single-molecule measurement) can happen through any one of these parallel pathways. Under

\*bxu@engr.uga.edu

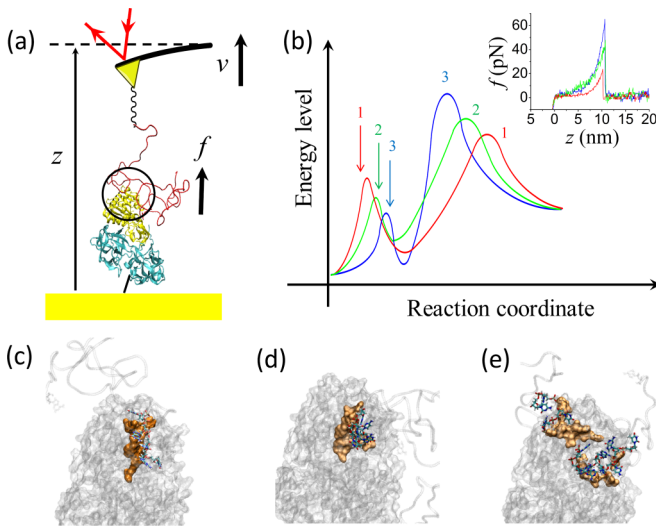


FIG. 1. (Color online) Schematics of the AFM DFS experiments measuring the unbinding force of the ricin-aptamer complex. (a) The ricin molecule was immobilized on the Au(111) surface via a cross-linker molecule. Under a constant velocity  $v$ , the AFM tip measured force  $f$  and distance  $z$ . (b) Schematic energy profiles for three unbinding pathways. Pathway 1 (labeled 1 in red) has the largest inner barrier and smallest outer barrier. Pathway 2 (labeled 2 in green) has the medium inner barrier and medium outer barrier. Pathway 3 (labeled 3 in blue) has the smallest inner barrier and largest outer barrier. The inset shows the representative  $f$ - $d$  curves for their corresponding unbinding pathways. Pathway 1 (in red) shows the smallest force peak, pathway 2 (in green) shows the middle force peak, and pathway 3 (in blue) shows the largest force peak. Structures in (c)–(e) show the predicted aptamer-ricin binding conformations for pathways 1–3, respectively. The predicted binding residues on ricin are shown in a surface representation (areas with darker color) and the predicted binding residues on aptamer are shown in a stick representation. The aptamer folding structures were simulated by AMBER [19]. The binding conformations were predicted by the HADDOCK web server [20].

loading rates higher than  $51.64 \text{ nN s}^{-1}$ , the thermal noise can broaden the force distributions and make it difficult to determine the most probable forces and their corresponding pathways. However, the loading rates we use, from  $0.24$  to  $600 \text{ nN s}^{-1}$ , are in ranges similar to those of other studies on multiple-pathway and multiple-barrier systems [24,25]. Therefore, the force and loading rate values obtained in our DFS experiments are sufficient to distinguish the unbinding force from noise.

It is important to first find the relationships among the peak values of the most probable forces and different binding conformations. The measured  $f$ - $d$  curves in DFS can be classified by each curve's proximity to the specific peak maximum of each force histogram. Gaussian distributions of all three peaks have overlapping parts, which make it impossible to determine to which peak (pathway) an individual  $f$ - $d$  curve belongs. However, if the unbinding force value of an  $f$ - $d$  curve is closer to a particular peak maximum in the force histogram, the curve has a higher probability of representing the unbinding pathway to which the histogram peak belongs. Therefore, the three most probable unbinding force values obtained in the force

histograms reveal the three most probable unbinding pathways. The smallest force value was postulated to be generated from the unbinding pathway (pathway 1) of the aptamer-loop III interactions, which has the smallest binding area on the top of the ricin A chain [Fig. 1(c)]. The largest force value may come from the loop I-loop III simultaneous unbinding (pathway 3), which shows two binding areas on the ricin surface [Fig. 1(d)]. The medium force value was proposed to belong to the loop I unbinding pathway (pathway 2), which has the active residues in the binding pocket of the ricin A chain [Fig. 1(e)].

After the binding conformations and their most probable unbinding forces have been connected under each loading rate, the energy profiles of those three unbinding pathways can be estimated by the Bell-Evans model. However, the measured  $f$ - $d$  curves, molecular dynamics simulations, and Bell-Evans model are not enough for a quantitative analysis of the complex relationships in this multiple-pathway system. We have developed a transition model to reveal the relationships among the changes of force histograms under different loading rates, the binding conformations, and the energy profiles of those three unbinding pathways.

## II. EXPERIMENTAL MEASUREMENTS

### A. Tip modification and sample preparation

The AFM tip was coated with  $15 \text{ nm}$  of gold film by an ion-beam-coating machine. Next, the gold-coated tip was immersed in  $2.0 \text{ mg/mL}$  polyethylene glycol (HS-PEG-COOH, molecular weight 2000) solution in dimethyl sulfoxide (DMSO) for  $3 \text{ h}$  (covered to avoid light). The linker molecule HS-PEG-COOH was attached to the gold surface by the gold-thiol reaction. In next step, a 1-(3-dimethylaminopropyl)-3-ethylcarbodiimide hydrochloride and  $N$ -hydroxysuccinimide mixture solution in water ( $10 \text{ mM}$  for each one) was used to activate the  $-\text{COOH}$  group on the top of the PEG linker. The  $5'$  terminal of the aptamer sequence was purchased with the attachment of an amine group by Integrated DNA Technologies (Coralville, IA, USA) [26]. After the tip was immersed in the solution of the amine-modified aptamer sequence [ $2.0 \mu\text{M}$  in phosphate buffered saline (PBS),  $\text{pH } 7.2$ ], the  $-\text{COOH}$  end of the PEG linker reacted with the amine end of the aptamer and formed a strong amide connection. This reaction occurred overnight at  $4 \text{ }^\circ\text{C}$  and the aptamer-modified tip was further washed with PBS ( $\text{pH } 7.2$ ) three times for AFM experiments.

The Au(111) surface was generated by hydrogen flaming. Next, a  $2.0 \text{ mg/mL}$  solution of linker molecule lipoic acid- $N$ -hydroxysuccinimide in DMSO was dropped on the Au(111) surface for  $2 \text{ h}$  to form a monolayer. After washing with DMSO and de-ionized water, a ricin solution ( $20 \text{ pg/mL}$ ) in PBS ( $\text{pH } 7.2$ ) was dropped on the modified Au(111) surface and kept at room temperature for  $1 \text{ h}$  [27,28]. Finally, the surface was washed with PBS ( $\text{pH } 7.2$ ) three times for AFM experiments.

### B. Atomic force microscopy force measurements and fittings of force histograms

Atomic force microscopy experiments were conducted in Top MAC mode (Agilent Technologies, Santa Clara, CA). The

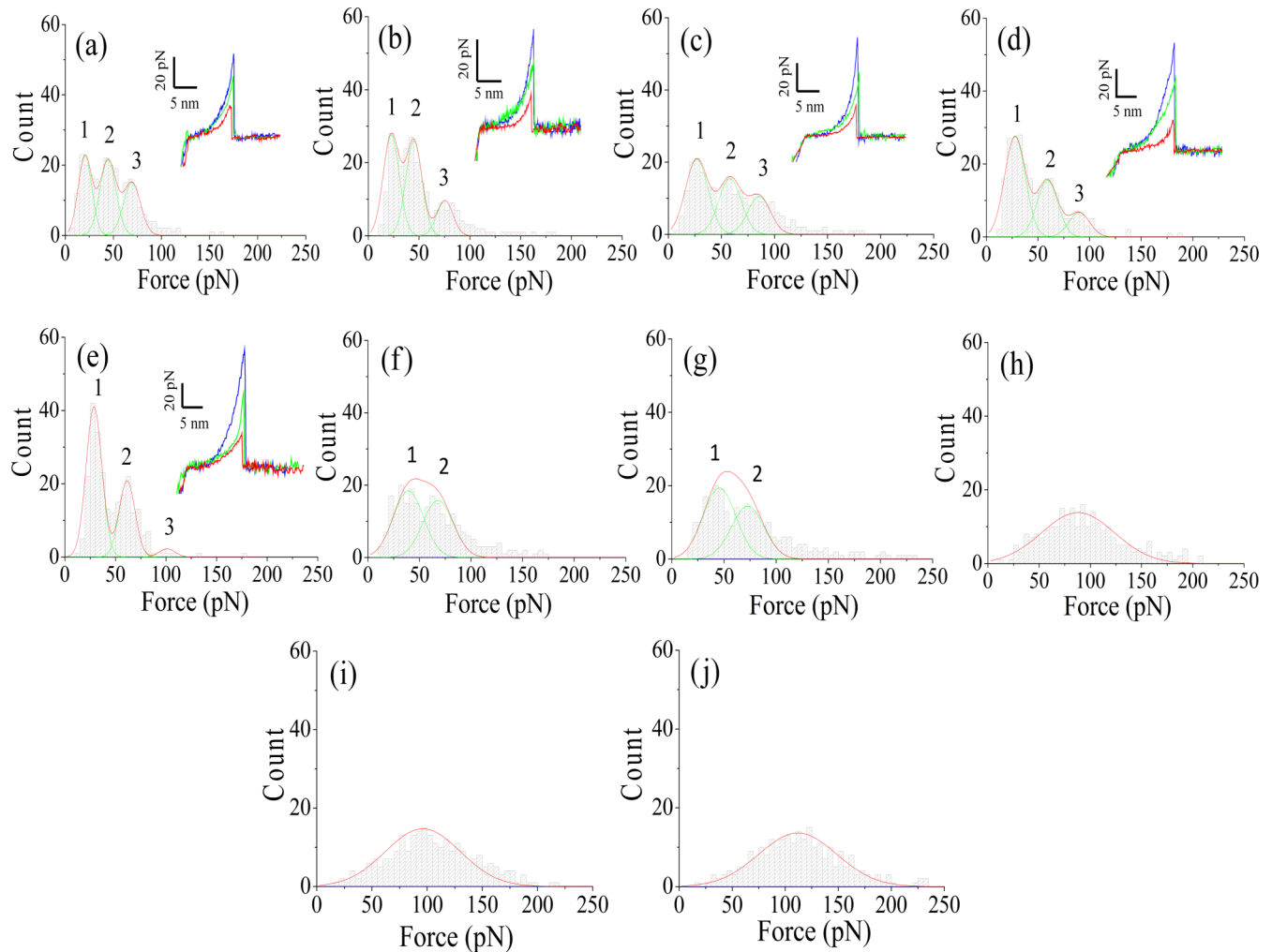


FIG. 2. (Color online) Force histograms and representative  $f$ - $d$  curves for (a) 0.24, (b) 2.72, (c) 15.37, (d) 38.02, (e) 51.64, (f) 82.06, (g) 100.0, (h) 200.0, (i) 400.0, and (j) 600.0  $\text{nN s}^{-1}$ . For insets (a)–(e), the  $f$ - $d$  curves for peak 1, pathway 1, and loop III unbinding are in red (smallest unbinding force in the inset). The  $f$ - $d$  curves for peak 2, pathway 2, and loop I unbinding are in green (medium unbinding force). The  $f$ - $d$  curves for peak 3, pathway 3, and loops I–III simultaneous unbinding are in blue (largest unbinding force).

immobilization of the ricin sample and the force measurements were conducted inside the liquid cell designed for the AFM instrument. The tip spring constant was 0.1 N/m. In PBS, pH 7.2, the measured resonant frequency under Top MAC mode was around 10 kHz. The DFS force measurements were done in this liquid cell, with 300  $f$ - $d$  curves collected under each loading rate. The loading rates were adjusted to certain values by changing the sweep duration and  $z$  position of the tip. The measured ricin molecules were selected from different areas of the sample surface.

Figure 2 shows the force histograms obtained under all ten loading rates, from 0.24 to 600  $\text{nN s}^{-1}$ . In this range the multiple energy barriers are distinguishable in the later  $F^*$  vs  $\ln R$  plots. The inset  $f$ - $d$  curves in Figs. 2(a)–2(e) were measured at the same distance but with different force values and the accumulation of this type of  $f$ - $d$  curve led to the multiple peaks in each force histogram.

Under the low loading rates (0.24–51.64  $\text{nN s}^{-1}$ ), the change of the peak areas of the three pathways is in a clear trend, which shows the redistribution processes of the unbinding reactions among the three different pathways. Peak

3 almost diminishes under 51.64  $\text{nN s}^{-1}$ . When the loading rate continues to increase, the third peak (peak 3) completely disappears and the other two peaks gradually merge to one peak. Under high loading rates (200.0–600.0  $\text{nN s}^{-1}$ ), only one peak exists in the histogram, which indicates that those unbinding pathways show certain relationships with the force applied to the binding complex. Under the medium range of loading rates (82.06–100  $\text{nN s}^{-1}$ ), the force histograms show two peaks, as shown in Figs. 2(f) and 2(g).

Based on the molecular docking and dynamics simulations, pathway 3 involves the most binding residues and largest binding area compared to the other two pathways, as shown in Fig. 1(e). Therefore, the binding-unbinding conformation for pathway 3 is supposed to require more time to stabilize and become increasingly rare with the increase of loading rates. Therefore, the two peaks under medium loading rates are assumed to represent pathways 1 and 2. Under medium and high loading rates, the force histograms all significantly broaden toward large force values, which is a common phenomenon in force spectroscopy [29]. Therefore, we consider all the small tails of the large force parts in those force

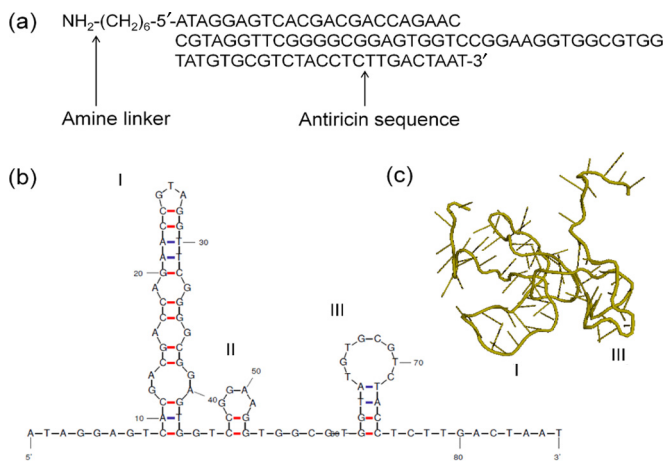


FIG. 3. (Color online) Aptamer sequence and folding structures. (a) Sequence modified by the amine functional group. (b) Secondary structure showing the three loops and stems formed by A-T and G-C base pairs. (c) The three-dimensional folding structure in a cartoon representation. The numbers I, II, and III show loops I, II, and III in (b) and (c).

histograms as the deviation caused by the thermal noise and measurement errors. The Gaussian fitting also neglects those parts of the force distribution under high loading rates and automatically fits two peaks under the loading rates of 82.06 and 100.0  $\text{nN s}^{-1}$ . Overall, both three-peak fittings under low loading rates (0.24–51.64  $\text{nN s}^{-1}$ ) and two-peak fittings under medium loading rates (82.06 and 100.0  $\text{nN s}^{-1}$ ) were determined by the same standards, not due to arbitrary selections. The in-depth explanation of these multiple peaks in force histograms under the low and medium loading rates will be described in Sec. IV with two force transition models.

### III. SIMULATIONS OF APTAMER FOLDING AND BINDING CONFORMATIONS

The aptamer sequence was obtained from the literature [26] and attached with a thiol group at the 5' end so that it can be attached to the gold-coated AFM tip [18]. The entire aptamer sequence including the 5' end amine functional group is  $\text{NH}_2\text{-(CH}_2\text{)}_6\text{-5'-ATAGGAGTCA-CGACGACCAG-AACCGTAGGT-TCGGGGCGGA-GTGGTCCGGA-AGGTGGCGTG-GTATGTGCGT-CTACCTCTTG-ACTAAT-3'}$ .

The secondary structure of the aptamer was predicted by the MFOLD webserver [30] and the tertiary folding structure was generated by the AMBER 11 molecular dynamic package [19]. Specifically, the program Nucleic Acid Builder in the AMBER package was used here to build the constraints on A-T and G-C base pairs, simulate equilibrium, and obtain the most stable folding structure. The structural information of this aptamer is shown in Fig. 3.

The ricin structure was obtained from Protein Data Bank entry 2AAI [31]. Before the docking simulation, both aptamer and ricin structures were neutralized and equilibrated in transferable intermolecular potential three-point water solvate box for 2 ns to obtain their most stable conformations in solution. Next, the ricin and aptamer structures were uploaded to the High Ambiguity Driven protein-protein DOCKing (HADDOCK) webserver [32,20] and the two loops of the aptamer were assigned as the active residues, respectively, in the first two docking simulations. In the third docking simulation, both loops were assigned as the active residues. The prediction of binding residues on the aptamer and ricin were based on the literature and molecular docking simulation. The HADDOCK webserver was used to search the active residues and form the most stable binding conformation. Then the loop III docking and the simultaneous dockings of loops I and III were tested and all of them showed stable binding conformations, as shown in Fig. 4. These docking simulations predicted that some ricin residues were involved in more than one pathway. For example, R125 is involved in all three pathways. Residues Y80, Y123, and R180 are involved in both the loop I binding and loop III binding, but not in the loop I–loop III simultaneous binding. Residue Q128 is involved in both the loop III binding and the loop I–loop III simultaneous binding, but not in the loop I binding. Moreover, the aptamer loops I and III also showed different binding residues for different binding conformations. For the loop I binding conformation, aptamer residues C23 to G28 bind to ricin. For the two-loop binding conformation, loop I residues A21 to T26 bind to ricin. For the loop III binding conformation, T66 to T70 bind to ricin, while G65 to C71 bind to ricin in the two-loop binding conformation. These overlaps and mismatches of ricin residues for aptamer loops I and III in different unbinding pathways indicate that the loop I–loop III simultaneous binding residues (or area) are not simply the addition of the ones from individual loops I and III binding. Therefore, these simulation results support a

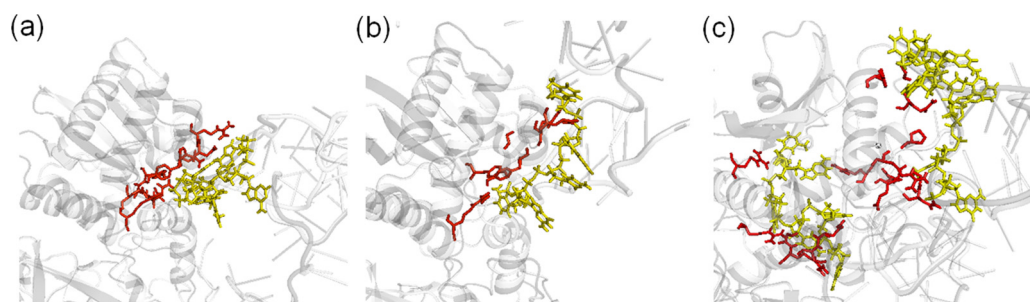


FIG. 4. (Color online) Predicted binding residues for different aptamer-ricin conformations: (a) loop I–ricin binding, (b) loop III–ricin binding, and (c) loops I–III binding simultaneously. The binding residues from ricin are in blue [stick representation in red (dark)] and the binding residues from aptamer are in green [stick representation in yellow (gray)]. The backbone structures of ricin and aptamer are gray and translucent (light gray), respectively.

transition model that can connect the three pathways together in a reaction network. In particular, based on the experimental data (Fig. 2), the change of loading rates influence the distributions of those three pathways, which started from their corresponding binding conformations shown in Fig. 6. Here the initial aptamer-ricin intermediate (revealed by high loading rates) is assumed to connect all three binding conformations. It will convert to one of these binding conformations under medium and low loading rates. These complex relationships among the different binding residues in different pathways are mainly due to the spatial constraints of ricin and aptamer folding structures. The details of the transition model are shown in Sec. IV.

#### IV. FORCE TRANSITION MODELS AND THEORIES

The development of the transition model was based on Markov analysis, which is a stochastic method used to study the time evolution of a system and describe its transition probabilities [33–35]. Markov models have been used to determine reaction properties by analyzing data obtained using fluorescence measurements [36–39]. However, previous research focused on stochastic properties of biomolecules evolving along the reaction time and was not specially developed for single-molecule experiments [35,40]. Our work focuses on the changing force distributions and their transition rates under different loading rates. The analysis is based on firsthand single-molecule experimental data and simulations of the binding conformations. When an external force is applied to the ricin-aptamer system under low loading rates ( $0.24\text{--}51.64\text{ nN s}^{-1}$ ), it reduces the activation energy barriers of pathways 1–3 according to the Bell-Evans model. This transition of the most probable unbinding force  $F^*$  starts with the loop I–loop III simultaneous unbinding pathway and connects all three pathways under low loading rates. Therefore, the change in force histograms reveals how individual unbinding reactions distribute among the three unbinding pathways. Based on simulations, the initial aptamer-ricin intermediate (revealed by high loading rates) is not like any one of the three binding conformations. Therefore, it will convert to one of these binding conformations under medium and low loading rates. These complex relationships among the different binding residues in different pathways are mainly due to the spatial constraints of ricin and aptamer folding structures. Based on the measured force data, pathway 3 has the strongest unbinding force and its energy barrier is expected to be higher than the other two pathways, so the unbinding process can easily transit to pathway 1 or 2. However, the redistribution of the unbinding process (or the change of probability) of pathway 1 or 2 to pathway 3 is much more difficult. We define  $S$  as the likelihood of the unbinding state of the molecular pair and  $K$  as the force transition rate of a certain pathway between two loading rates. We assume that pathways 1 and 2 cannot transit to pathway 3, so the  $K$  values of pathways 1 and 2 into themselves are unity (100%).

Under different loading rates, the changes of energy landscapes under the applied forces cause the redistribution of the likelihood ( $S_1$ ,  $S_2$ , and  $S_3$ ) for each pathway. Therefore, the observed shifts of peak area values between two force histograms under different loading rates are related to the

unbinding pathways. A single-molecule unbinding reaction can be simply put as  $S_0 \rightleftharpoons S_1$ , where  $S_0$  is the likelihood of the binding state of the molecular pair and  $S_1$  is the likelihood of the unbinding state. Using  $k_1$  (in %) as the forward rate constant and  $k_0$  (in %) as the backward rate constant, the master equation of this reaction can be written as

$$\frac{dS_0}{dt} = -k_1(t)S_0(t) + k_0(t)S_1(t). \quad (1)$$

In AFM DFS experiments the two molecules move apart much faster than their diffusion in the solution, so the rebinding term  $k_0S_1$  goes to zero. We define the constant tip velocity as  $v$  and the distance as  $vdt$  and the overall spring constant of the AFM tip is simplified as  $\kappa_s$ . The force and distance follow Hook's law

$$df = \kappa_s v dt. \quad (2)$$

Now  $df$  can be substituted into the simplified master equation

$$\frac{dS_0}{dt} = -k_1(t)S_0(t) \quad (3)$$

to obtain

$$\frac{dS_0}{df} = -\frac{k_1}{\kappa_s v} S_0. \quad (4)$$

Here we assume that Hook's law holds for every loading rate [41]. Generally, a higher loading rate will generate a bigger force to break the bond and this bigger force should be equivalent to the stochastic process if the  $f$ - $d$  curve occurs in continuous time. Therefore, we use Eq. (4) to connect the unbinding force values from two loading rates. When the most probable unbinding force changes during the transition process, we define the force transition rate to be  $k_{f1} = \frac{k_1}{K_s v}$  (in %  $\text{N}^{-1}$ ). Substituting it into Eq. (4) yields

$$\frac{dS_0}{df} = -k_{f1} S_0. \quad (5)$$

Equation (5) describes the relationship between the force transition rate and the likelihood of the binding state caused by the changes of the applied force from the AFM tip. The integral of Eq. (5) from one force value to another (new) force value yields

$$\Delta S_0 = e^{-k_{f1} \Delta f}. \quad (6)$$

The force changes in DFS are usually on the pN scale, so we assume that the linear approximation of Eq. (6) is valid under the DFS experimental conditions:

$$\Delta S_0 = 1 - k_{f1} \Delta f. \quad (7)$$

Because the change of DFS loading rates results in the corresponding change of unbinding forces, the likelihood of one unbinding reaction through its pathway can be considered a function of the loading rates. The unbinding energy barrier of that certain reaction is lowered by the applied force, so the  $k_{f1}$  value can be considered as the mechanical property of a certain unbinding reaction with the change of loading rates. For a system with three pathways, a transition matrix  $T$  can be used to connect all  $k_f$  of the different pathways together, as

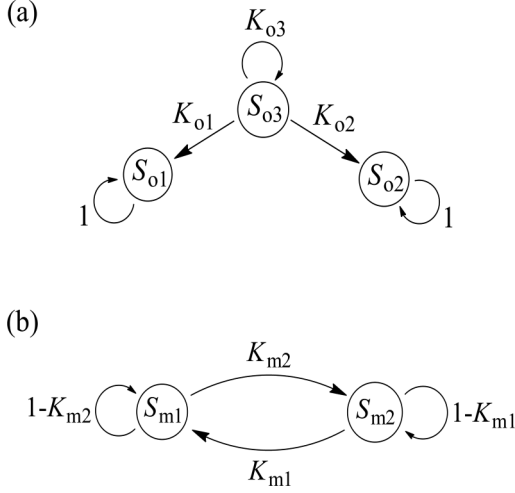


FIG. 5. Transition diagrams for multiple unbinding pathways. (a) Transition diagram under low loading rates (0.24–51.64 nN s<sup>-1</sup>). Here  $S_{o1}$ ,  $S_{o2}$ , and  $S_{o3}$  represent the likelihood of going through each unbinding pathway under a certain loading rate. (b) Transition diagram under medium loading rates (82.06–100 nN s<sup>-1</sup>).

shown by

$$\frac{d[S_0]}{df} = -[T][S_0]. \quad (8)$$

Using a similar approximation for Eqs. (6) and (7), Eq. (8) can be transformed into

$$[S_{f1}] \times [T] = [S_{f2}]. \quad (9)$$

Here the matrix  $[T]$  includes parameters such as  $k_{f1}$  and  $\Delta f$ . The matrices  $[S_{f1}]$  and  $[S_{f2}]$  represent the likelihood of the binding states of the three pathways under two applied forces  $f1$  and  $f2$ , which correspond to two different loading rates. The change of DFS loading rate changes the applied force value. This change of the applied force in turn changes the energy landscapes of those pathways and caused the redistribution of the likelihood ( $S_1$ ,  $S_2$ , and  $S_3$ ) for each pathway under the applied force. Therefore, the observed shifts of peak area values between two force histograms under different loading rates are related to the unbinding pathways. The transition diagram of this process is shown in Fig. 5(a) and the matrix analysis of this transition model can be written as

$$[S_{1,i}, S_{2,i}, S_{3,i}] \begin{bmatrix} 1 & 0 & 0 \\ 0 & 1 & 0 \\ K_{o1} & K_{o2} & K_{o3} \end{bmatrix} = [S_{1,j}, S_{2,j}, S_{3,j}]. \quad (10)$$

Here  $S$  is the normalized peak area value from the force histogram; the subscripts 1, 2, and 3 represent pathways 1, 2, and 3, and  $i$  and  $j$  denote the initial and final loading rates from the DFS experiments, respectively. The middle part of Eq. (10) is the matrix  $[T]$  in Eq. (9), where  $K_{o1}$ ,  $K_{o2}$ , and  $K_{o3}$  are the matrix transition rates for their corresponding unbinding pathways. Here  $o$  represents the outer energy barriers revealed by the force-distance measurements under relatively low loading rates, according to the Bell-Evans multiple-barrier model. The  $K_{o1}$ ,  $K_{o2}$ , and  $K_{o3}$  are defined as  $k_f \Delta f$ . Here

$k_f$  is the force transition rate per unit of force. The  $\Delta f$  is the change of the most probable unbinding force of each pathway (pathway 1, 2, or 3) between the starting loading rate and the ending loading rate in Eq. (10). Therefore, the  $K_{o1}$ ,  $K_{o2}$ , and  $K_{o3}$  values obtained in Eq. (10) are not from the analytical solutions of the derivative equations for each reaction pathway. Instead, these values are estimated from the linear approximation (using the transition matrix) of the force transition process between the starting loading rate and the ending loading rate. Equation (10) connects the values of corresponding peak areas in the two force histograms under two different loading rates.

Under the medium range of loading rates (82.06–100 nN s<sup>-1</sup>), the force histograms shows only two peaks for pathways 1 and 2. A new transition matrix is necessary to describe the redistribution of the likelihood ( $S_1$  and  $S_2$ ) for each pathway. This transition process is shown in Fig. 5(b) and the matrix analysis under medium loading rate can be written as

$$[S_{1,i}, S_{2,i}] \begin{bmatrix} 1 - K_{m2} & K_{m2} \\ K_{m1} & 1 - K_{m1} \end{bmatrix} = [S_{1,j}, S_{2,j}]. \quad (11)$$

Here  $S$  is the normalized peak area value from the force histogram and the subscripts 1 and 2 represent pathways 1 and 2. The subscripts  $i$  and  $j$  represent the initial and final loading rates, respectively. The parameters  $K_{m1}$  and  $K_{m2}$  are the matrix transition rates for their corresponding unbinding pathways under medium loading rates.

Figure 6 shows the overall reaction network for the ricin-aptamer interactions under different loading rates. This model is based on the histograms of unbinding forces at loading rates ranging from 0.24 to 600 nN s<sup>-1</sup> (Fig. 2). Under high loading rates, the inner energy barrier dominates each unbinding pathway, while the outer energy barrier dominates the pathway when the force measurements are under low loading rates. The transition mode changes under the medium loading rates. This change of transition mode [from Figs. 5(a) to 5(b)] is caused by the change of relative positions of energy profiles for each pathway. The transition models in Fig. 5 form the reaction network in Fig. 6 and the kinetic parameters such

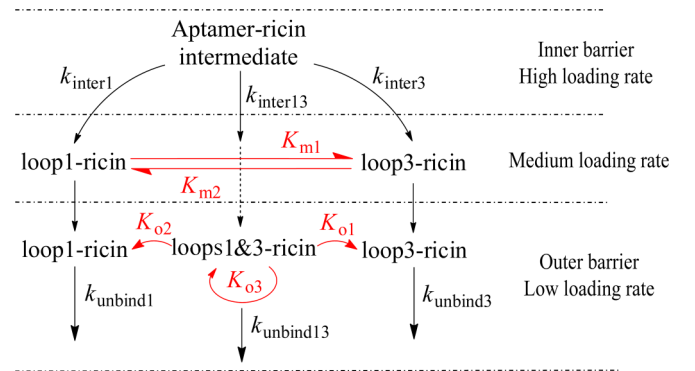


FIG. 6. (Color online) Overall reaction network showing the unbinding pathways (black, all in the vertical direction) under different ranges of loading rates and transition processes with the applied force (red, in the horizontal direction, marked with  $K_{m1}$ ,  $K_{m2}$ ,  $K_{o1}$ ,  $K_{o2}$ , and  $K_{o3}$ ), which follow the transition models in Figs. 5(a) and 5(b).

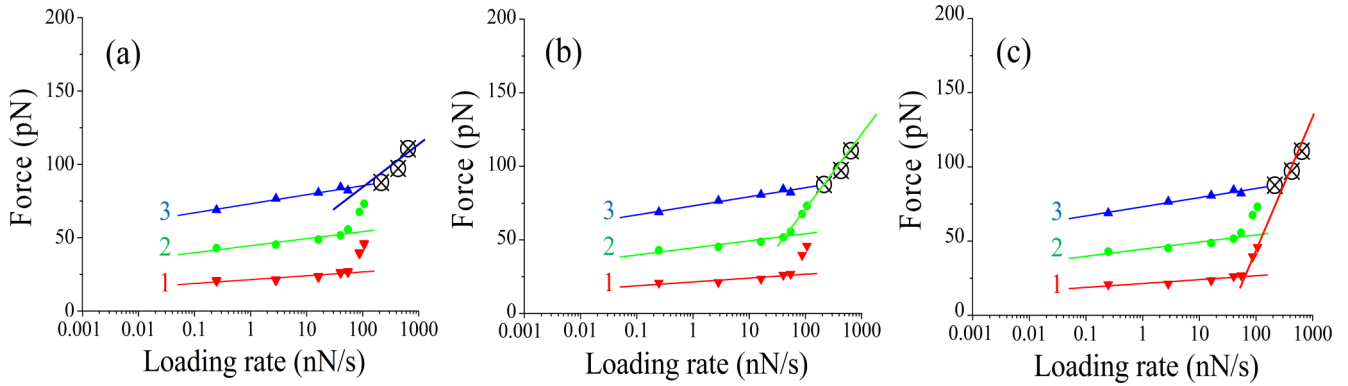


FIG. 7. (Color online) Plots of  $F^*$  vs  $\ln R$  for the three unbinding pathways. Force peak values were obtained by Gaussian fitting from the histograms. In the two-barrier fitting, the plots and data points for the loop I pathway are labeled 2 (green circles), those for the loop III pathway are labeled 1 (inverted red triangles), and those for the loop I–loop III pathway are labeled 3 (blue triangles). The shared data points at high loading rates 200.0, 400.0, and 600.0  $\text{nN s}^{-1}$  are marked as crossed circles.

as the reaction rate constants in this reaction network can be determined by Bell-Evans model, which connects the applied force with the energy profile of each pathway. Therefore, the force transition processes among the three pathways are connected to the energy profiles of those pathways. We analyze further the energy profiles involved in this multiple-pathway system in order to quantitatively explain the mechanism behind the relative energy levels of those pathways and the transitions among them.

### V. QUANTITATIVE ANALYSIS OF THE ENERGY PROFILES

#### A. Fitting of $F^*$ vs $\ln R$ plots to estimate the off rates and energy profiles

The fittings of  $F^*$  vs  $\ln R$  plots are based on Bell-Evans multiple-barrier model [21]. Under the low loading rates from 0.24 to 51.64  $\text{nN s}^{-1}$ , each pathway has three peak values in the force histograms. So the fitted plots are clearly separated from each other in Figs. 7(a)–7(c). Under medium loading rates 86.02 and 100.0  $\text{nN s}^{-1}$ , the loop I–loop III pathway no longer shows in the force histograms, so no data point is available for this pathway in this range. For the other two pathways, the data points clearly indicate new slopes for their fitted plots. Under high loading rates 200.0–600  $\text{nN s}^{-1}$ , only one peak shows in

each force histogram, which is assumed to represent the initial aptamer-ricin intermediate complex that generates these three pathways, as shown in Fig. 6. In order to estimate the second slope of the individual pathway, the fitting starting from the end of the first slope (51.64  $\text{nN s}^{-1}$ ) includes the medium range and high range of the loading rates. The changing of slopes around 51.64  $\text{nN s}^{-1}$  indicates the change of reaction mechanisms. The new mechanism is for the inner barrier reaction.

Therefore, the first fitting range is from 0.24 to 51.64  $\text{nN s}^{-1}$ , totaling five points for each pathway. The second fitting range is from 51.64 to 600.0  $\text{nN s}^{-1}$ , totaling four points for the loop I–loop III pathway and in total six points for each of the other two pathways. The fit values are shown in Table I. The off rates of the outer barriers are calculated as  $(6.6 \pm 1.7) \times 10^{-6}$ ,  $(2.6 \pm 0.6) \times 10^{-7}$ , and  $(5.8 \pm 0.6) \times 10^{-10} \text{ s}^{-1}$  for pathways 1, 2, and 3, respectively. The off rates of the inner barriers are calculated as  $(6.9 \pm 2.3) \times 10^2$ ,  $(1.6 \pm 0.08) \times 10^2$ , and  $2.6 \pm 0.2 \text{ s}^{-1}$  for pathways 1, 2, and 3, respectively. For each unbinding pathway, the off rates of inner energy barriers and outer energy barriers are significantly different, which indicates that the unbinding process to overcome the inner energy barrier is happening much more easily and more frequently. These energy estimates help us understand the detailed structural-function relationships of the aptamer-ricin complexes shown in Figs. 1 and 4.

TABLE I. Fit values for each  $F^*$  vs  $\ln R$  plot in Fig. 7.

Barrier	Parameter	Pathway 1 Loop III	Pathway 2 Loop I	Pathway 3 Loops I–III
outer	slope ( $10^{-3} \text{ pN}$ )	$1.145 \pm 0.29$	$2.094 \pm 0.49$	$2.693 \pm 0.30$
outer	Y-axis intercept (pN)	$21.42 \pm 0.83$	$44.62 \pm 1.39$	$73.21 \pm 0.85$
outer	$k_{\text{off}}$ ( $\text{s}^{-1}$ )	$(6.6 \pm 1.7) \times 10^{-6}$	$(2.6 \pm 0.6) \times 10^{-7}$	$(5.8 \pm 0.6) \times 10^{-10}$
outer	$x_\beta$ (nm)	$3.58 \pm 0.91$	$1.95 \pm 0.46$	$1.52 \pm 0.17$
outer	$\Delta E$ ( $k_B T$ )	$11.9 \pm 1.1$	$15.1 \pm 1.1$	$21.3 \pm 0.2$
inner	slope ( $10^{-3} \text{ pN}$ )	$10.46 \pm 3.52$	$21.13 \pm 1.11$	$35.67 \pm 3.39$
inner	Y-axis intercept (pN)	$-34.42 \pm 19.35$	$-171.9 \pm 13.38$	$-360.6 \pm 40.79$
inner	$k_{\text{off}}$ ( $\text{s}^{-1}$ )	$(6.9 \pm 2.3) \times 10^2$	$(1.6 \pm 0.08) \times 10^2$	$2.6 \pm 0.2$
inner	$x_\beta$ (nm)	$0.11 \pm 0.04$	$0.19 \pm 0.01$	$0.39 \pm 0.04$
inner	$\Delta E$ ( $k_B T$ )	$-0.9 \pm 1.2$	$-5.1 \pm 1.0$	$-6.5 \pm 1.0$

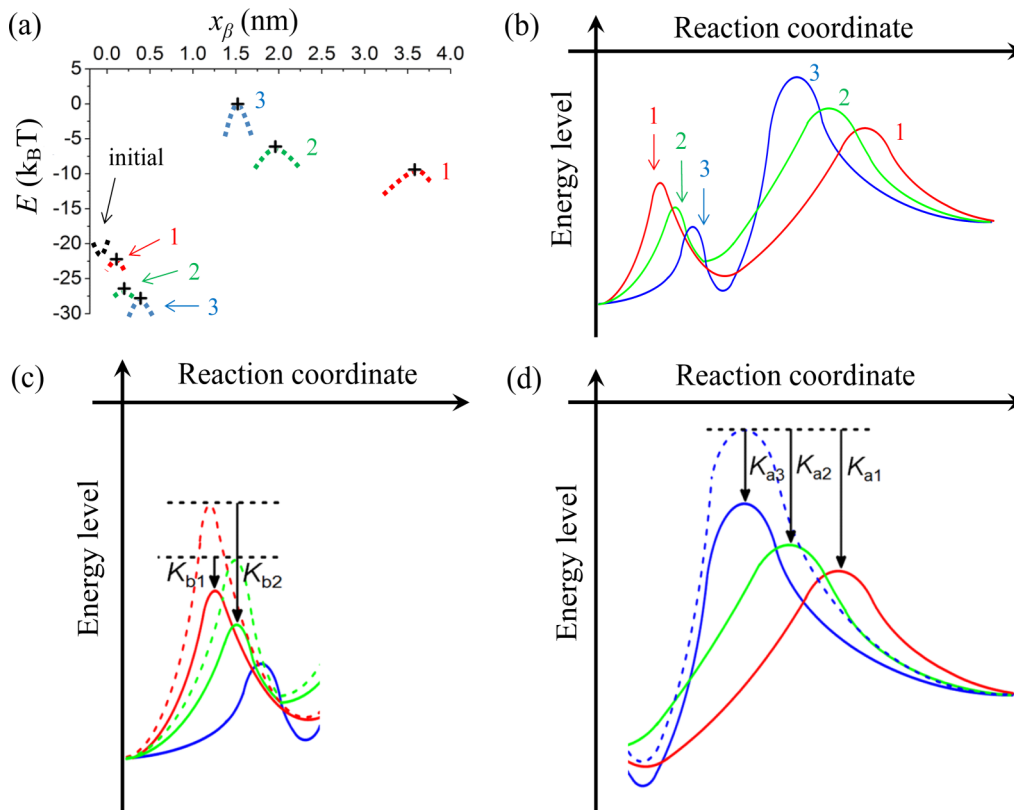


FIG. 8. (Color online) Estimate of energy levels. (a) Reconstructed energy landscapes of the ricin-aptamer unbinding pathway. Pathway 1 (labeled 1 in red) has the highest energy level of all inner barriers and the lowest energy level of the outer barriers. Pathway 3 (labeled 3 in blue) has the lowest energy level of all inner barriers and the highest energy level of the outer barriers. Pathway 2 (labeled 2 in green) has the medium energy level between pathways 1 and 3. The “initial” labeled in black at  $x_\beta = 0.0$  represents the estimated value of the initial energy level of the binding state  $-22k_B T$ . (b) The schematic energy profiles of ricin-aptamer unbinding pathways with the transitions among them. (c) Transitions between pathways 1 and 2 for the inner energy barrier, with their corresponding transition constants  $K_{b1}$  and  $K_{b2}$ , respectively. (d) Transitions from pathway 3 to pathways 1, 2, and 3 for the outer energy barrier, with their corresponding transition constants  $K_{a1}$ ,  $K_{a2}$ , and  $K_{a3}$ , respectively. In (b) and (c), the dashed curves show the energy profiles of the starting loading rates and the solid curves show the energy profiles of the ending loading rates. The transition inside each pathway is not shown.

Figure 8(a) shows the reconstructed energy landscape of each unbinding pathway using the Bell-Evans model [21,42]. Although the ricin-aptamer binding complex has three conformations, the energy levels at their initial binding states are assumed to be very similar, as the black dashed curve at  $x_\beta = 0$  shows. The initial energy level of the binding state is estimated using a microscopic diffusive relaxation time of  $4.2 \times 10^{-9}$  s according to the literature [21,43]. The binding state energy value is estimated to be around  $-22k_B T$  [42,44].

Next, the outer and inner energy barriers  $E$  along the reaction course  $x_\beta$  of these three unbinding pathways are calculated using the Bell-Evans multiple-barrier model (see Table I). For outer energy barriers, pathway 1 shows the lowest barrier energy [red curve,  $(11.9 \pm 1.1)k_B T$  above initial binding state] and longest barrier locations ( $3.6 \pm 0.9$  nm), pathway 3 shows the highest energy barrier [blue curve,  $(21.3 \pm 0.2)k_B T$  above initial binding state] and shortest barrier position ( $1.5 \pm 0.2$  nm), and pathway 2 has the medium energy barrier [green curve,  $(15.1 \pm 1.1)k_B T$  above initial binding state] and medium barrier position ( $2.0 \pm 0.5$  nm).

Based on the experimental data, pathway 1 (i.e., loop III binding) shows relatively large errors for  $x_\beta$  values, which are

the major contribution to the errors of energy levels. Especially for the inner barrier of pathway 1, the error  $\pm 1.2k_B T$  is even greater than the energy level  $-0.9k_B T$ . The main reason is that the external applied forces under large loading rates generate bigger noise during the measurements of weak unbinding forces of pathway 1. For the other two pathways, their stronger unbinding forces reduce the errors on the estimates of barrier width  $x_\beta$  and energy level  $\Delta E$ .

For inner energy barriers, pathway 1 shows the highest energy level [red,  $(0.9 \pm 1.2)k_B T$  below initial binding state, barrier position at  $0.1 \pm 0.04$  nm], pathway 3 shows the lowest energy level [blue,  $(6.5 \pm 1.0)k_B T$  below the initial binding state, barrier position at  $0.4 \pm 0.04$  nm], and pathway 2 is still in the middle [green,  $(5.0 \pm 1.0)k_B T$  below initial binding state, barrier position at  $0.2 \pm 0.01$  nm]. The relative energy value and barrier positions of these pathways are comparable to other biomolecular interactions [21]. However, the three inner barrier energy levels are slightly higher than the estimated  $-22k_B T$  and the real value cannot be directly determined by single-molecule measurements [44]. Previous literature investigated the transition path times and diffusion of nucleic acids and proteins across their folding-unfolding barriers, but

we cannot find a practical method to obtain experimentally the initial binding energy level [3,45]. Therefore, we use the value of  $-22k_B T$  as a rough reference for this ricin-aptamer system.

Based on the binding conformations of the three pathways, the conformation for pathway 3 [Fig. 1(e)] shows the most binding residues and two binding sites for ricin and aptamer. Therefore, the unbinding process is expected to generate a bigger force and shorter length of the barrier. In contrast, the conformation for pathway 1 [Fig. 1(c)] has the fewest binding residues and smallest binding area, which leads to the smallest unbinding force and most flexible structural change, and the longest barrier location. For the inner barriers, we assume that pathway 1 (red) had the most similar binding conformation to the initial conformation of the binding intermediate, so its barrier level is also the closest to the initial binding state. Therefore, the initial binding complex needs to move a longer distance (and  $x_\beta$ ) to reach the binding-unbinding conformations of the other two pathways (green and blue), so the inner energy barriers of these two pathways differ greater still from the initial binding state. Figure 8(b) shows the schematic energy profiles for all three unbinding pathways and the transitions of unbinding reactions from the starting loading rate to the ending loading rate caused by the applied forces. The force transition rates marked in Figs. 8(c) and 8(d) are the same ones used in Fig. 5. These schematic energy profiles summarize the two transition models (for inner and outer energy barriers) in the perspective of reaction energy and help us understand the transitions in Fig. 5.

### B. Changes of energy levels during transitions

Finally, based on the peak areas obtained by the DSF experiments, we calculate the matrix transition rates of the three pathways ( $K_1$ ,  $K_2$ , and  $K_3$ ) for the four transition processes that happened under loading rates from 0.24 to 51.64 nNs<sup>-1</sup>, according to Eq. (10). The  $K$  values represent the percentage of unbinding events when pathway 3 transitioned to pathway 1 or 2, or remained in pathway 3, between two loading rates where different external forces are applied. The unbinding events in pathways 1 and 2 always stay in their own pathways, as previously discussed. The energy difference caused by the transition between two pathways ( $\Delta\Delta E$ ), from a starting loading rate  $i$  to an ending loading rate  $i+1$ , can be estimated from the  $K$  values. According to the Arrhenius relationship, the off rate under the applied force  $k_{\text{off}}(F)$  and

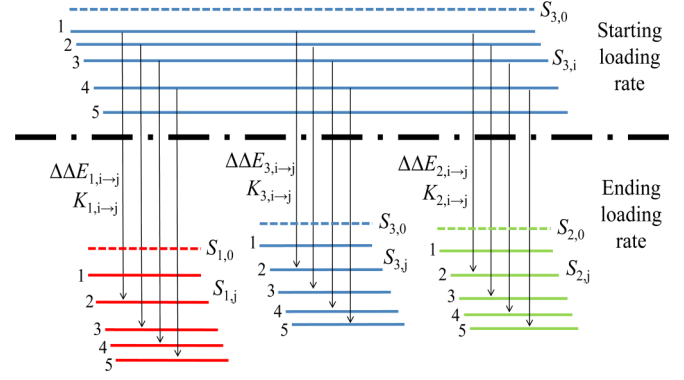


FIG. 9. (Color online) Relationships between different transitions following the changes of loading rates: pathway 1 in red (lower left part), pathway 2 in green (lower right part), and pathway 3 in blue (upper part as the starting state and lower middle part as the ending state).

the off rate under zero force  $k_{\text{off}}(0)$  can be expressed as

$$\frac{k_{\text{off}}(F)}{k_{\text{off}}(0)} = e^{F x_\beta / k_B T}. \quad (12)$$

For the transition between pathways 3 and 1, from loading rates  $i$  to loading rate  $i+1$ ,

$$\begin{aligned} \ln \left( \frac{k_{\text{off},1}(F_{i+1})k_{\text{off},3}(0)}{k_{\text{off},1}(0)k_{\text{off},3}(F_i)} \right) &= \frac{F_{i+1}x_{\beta,1,i+1} - F_i x_{\beta,3,i}}{k_B T} \\ &= \frac{\Delta\Delta E_{3 \rightarrow 1}}{k_B T}. \end{aligned} \quad (13)$$

Here the  $k_{\text{off},3}(0)$  and  $k_{\text{off},1}(0)$  are the off rates of pathways 3 and 1, respectively, under zero force. The  $k_{\text{off},3}(F_i)$  is the off rates value of pathway 3 under applied force  $F_i$ , while  $k_{\text{off},1}(F_{i+1})$  is the off rate value of pathway 1 under applied force  $F_{i+1}$ . These off rate values under certain applied force (loading rate) are calculated using the Bell-Evans model. Here  $\Delta\Delta E_{3 \rightarrow 1}$  is the energy difference (in the unit of  $k_B T$ ) caused by the transition process. The same relationships are also available for the transitions from pathway 3 to pathway 2 and from pathway 3 to 3, under two continuous loading rates (Fig. 9). The calculated  $\Delta\Delta E$  values for three pathways under different loading rates ( $K_1$ ,  $K_2$ , and  $K_3$ ) are shown in Table II. Table II further provides quantitative information for the change of energy barriers. For example, Table II

TABLE II. Force transition rate  $K$  and energy changes caused by transitions among different pathways ( $\Delta\Delta E$ ). Here  $K_1$ ,  $K_2$ , and  $K_3$  represent the force transition rate values of pathways 1, 2, and 3, respectively.

Transition	Force transition rate (%)			$\Delta\Delta E$ ( $k_B T$ )		
	$K_1$	$K_2$	$K_3$	Pathway 3 to 1	Pathway 3 to 2	Pathway 3 to 3
0.24–2.72 nN s <sup>-1</sup>	0.096	0.056	0.848	a	a	a
2.72–15.37 nN s <sup>-1</sup>	0.129	0.054	0.817	-7.3	-4.4	1.7
15.37–38.02 nN s <sup>-1</sup>	0.238	0.240	0.522	-7.8	-3.7	0.46
38.02–51.64 nN s <sup>-1</sup>	0.379	0.272	0.349	-8.6	-5.7	-0.10
51.64–81.02 nN s <sup>-1</sup>	0.502	0.553	b			
81.02–100.0 nN s <sup>-1</sup>	0.502	0.553	b			

<sup>a</sup>Energy comparison is not applicable for the first transition process.

<sup>b</sup>The force transition rate  $K_3$  is not applicable in the transition model under the medium loading rates.

shows that  $\Delta\Delta E_{3-1}$  and  $\Delta\Delta E_{3-2}$  are always negative, so these transitions under increasing forces (or loading rates from 0.24 to 51.64 nN s<sup>-1</sup>) release energy. However,  $\Delta\Delta E_{3-3}$  is first positive at low loading rate, changing to negative at high loading rate, so this transition process consumes small amounts of energy under low loading rates, but releases energy under high loading rates.

The applied force changes the energy landscapes of all three unbinding pathways. Table II shows that  $\Delta\Delta E_{3-1}$  and  $\Delta\Delta E_{3-2}$  are always negative, so these transitions under increasing forces (or loading rates from 0.24 to 51.64 nN s<sup>-1</sup>) release energy. However,  $\Delta\Delta E_{3-3}$  is first positive at low loading rate and changes to negative at high loading rate, so this transition process consumes small amounts of energy under low loading rates, but releases energy under high loading rates.

## VI. CONCLUSION

We presented a transition model combining the conventional Bell-Evans model and Markov-type transition matrix to

analyze single-molecule ricin-aptamer interactions measured by AFM DFS. Based on distributions of unbinding forces and molecular dynamics, multiple unbinding pathways were connected in an overall reaction model with their corresponding force transition constants. This model quantitatively described the complex behaviors of single-protein and aptamer molecules under external forces and transition relationships among multiple unbinding pathways. This approach provides detailed information hidden in the DFS experimental data of complex protein-DNA interactions. This approach can be used to study other single-molecule interactions, especially those with multiple reaction pathways.

## ACKNOWLEDGMENTS

We thank J. Hamill for reading the manuscript and discussion. This work was supported by the National Science Foundation through Grants No. CBET 1139057 and No. ECCS 1231967.

- 
- [1] L. Saiz, *J. Phys.: Condens. Matter* **24**, 193102 (2012).  
 [2] J. H. J. Hoeijmakers, *N. Engl. J. Med.* **361**, 1475 (2009).  
 [3] H. Yu, X. Liu, K. Neupane, A. N. Gupta, A. M. Brigley, A. Solanki, I. Sosova, and M. T. Woodside, *Proc. Natl. Acad. Sci. U.S.A.* **109**, 5283 (2012).  
 [4] D. H. Paik and T. T. Perkins, *Angew. Chem. Int. Ed. Engl.* **51**, 1811 (2012).  
 [5] M. Held and F. Noe, *Eur. J. Cell Biol.* **91**, 357 (2012).  
 [6] N. C. Harris, Y. Song, and C.-H. Kiang, *Phys. Rev. Lett.* **99**, 068101 (2007).  
 [7] G. I. Bell, *Science* **200**, 618 (1978).  
 [8] C. Jarzynski, *Phys. Rev. Lett.* **78**, 2690 (1997).  
 [9] S. Guo, C. Ray, A. Kirkpatrick, N. Lad, and B. B. Akhremitchev, *Biophys. J.* **95**, 3964 (2008).  
 [10] T. Erdmann, S. Pierrat, P. Nassoy, and U. S. Schwarz, *Europhys. Lett.* **81**, 48001 (2008).  
 [11] D. Leckband, *Annu. Rev. Biophys. Biomol. Struct.* **29**, 1 (2000).  
 [12] A. M. Berezhkovskii, *J. Chem. Phys.* **134**, 074114 (2011).  
 [13] U. Seifert, *Phys. Rev. Lett.* **84**, 2750 (2000).  
 [14] M. Manosas, I. Junier, and F. Ritort, *Phys. Rev. E* **78**, 061925 (2008).  
 [15] Z. Yu, V. Gaerig, Y. Cui, H. Kang, V. Gokhale, Y. Zhao, L. H. Hurley, and H. Mao, *J. Am. Chem. Soc.* **134**, 5157 (2012).  
 [16] Y. Zhao and G. D. Stormo, *Nat. Rev. Genet.* **11**, 751 (2010).  
 [17] J. Audi, M. Belson, M. Patel, J. Schier, and J. Osterloh, *J. Am. Med. Assoc.* **294**, 2342 (2005).  
 [18] B. Wang, C. Guo, G. Chen, B. Park, and B. Xu, *Chem. Commun.* **48**, 1644 (2012).  
 [19] D. A. Case *et al.*, AMBER 11 (University of California, San Francisco, 2010).  
 [20] S. J. de Vries, M. van Dijk, and A. M. J. J. Bonvin, *Nat. Protoc.* **5**, 883 (2010).  
 [21] E. Evans, *Biophys. Chem.* **82**, 83 (1999).  
 [22] E. Evans, *Annu. Rev. Biophys. Biomol. Struct.* **30**, 105 (2001).  
 [23] A. Fuhrmann, S. Getfert, Q. Fu, P. Reimann, S. Lindsay, and R. Ros, *Biophys. J.* **102**, 2381 (2012).  
 [24] C. Ray, J. R. Brown, and B. B. Akhremitchev, *J. Phys. Chem. B* **111**, 1963 (2007).  
 [25] A. Noy, *Curr. Opin. Chem. Biol.* **15**, 710 (2011).  
 [26] J. Tang, J. Xie, N. Shao, and Y. Yan, *Electrophoresis* **27**, 1303 (2006).  
 [27] G. Chen, J. Zhou, B. Park, and B. Xu, *Langmuir* **25**, 2860 (2009).  
 [28] G. Chen, J. Zhou, B. Park, and B. Xu, *Appl. Phys. Lett.* **95**, 043103 (2009).  
 [29] E. Evans and K. Ritchie, *Biophys. J.* **72**, 1541 (1997).  
 [30] M. Zuker, *Nucleic Acids Res.* **31**, 3406 (2003).  
 [31] E. Rutenber, B. J. Katzin, S. Ernst, E. J. Collins, D. Mesna, M. P. Ready, and J. D. Rovertus, *Proteins* **10**, 240 (1991).  
 [32] M. van Dijk, A. D. J. van Dijk, V. Hsu, R. Boelens, and A. M. J. J. Bonvin, *Nucleic Acids Res.* **34**, 3317 (2006).  
 [33] D. T. Gillespie, *Physica A* **188**, 404 (1992).  
 [34] M. R. Hoare, *Nature (London)* **226**, 599 (1970).  
 [35] N. T. Schmandt and R. F. Galan, *Phys. Rev. Lett.* **109**, 118101 (2012).  
 [36] D. A. Smith, W. Steffen, R. M. Simmons, and J. Sleep, *Biophys. J.* **81**, 2795 (2001).  
 [37] J. Shuai and P. Jung, *Biophys. J.* **83**, 87 (2002).  
 [38] S. C. Kou, X. S. Xie, and J. S. Liu, *J. Roy. Stat. Soc. C (Appl. Statist.)* **54**, 469 (2005).  
 [39] J. Stigler, F. Ziegler, A. Gieseke, J. C. Gebhardt, and M. Rief, *Science* **334**, 512 (2011).  
 [40] T. E. Turner, S. Schnell, and K. Burrage, *Comput. Biol. Chem.* **28**, 165 (2004).  
 [41] A. R. Bizzarri and S. Cannistraro, *Chem. Soc. Rev.* **39**, 734 (2010).  
 [42] R. Merkel, P. Nassoy, A. Leung, K. Ritchie, and E. Evans, *Nature (London)* **397**, 50 (1999).  
 [43] B. Tinland, A. Pluen, J. Sturm, and G. Weill, *Macromolecules* **30**, 5763 (1997).  
 [44] H. Grubmüller, B. Heymann, and P. Tavan, *Science* **271**, 997 (1996).  
 [45] K. Neupane, D. B. Ritchie, H. Yu, D. A. N. Foster, F. Wang, and M. T. Woodside, *Phys. Rev. Lett.* **109**, 068102 (2012).